

Job-Sharing Charge Storage in a Mixed Ion/Electron Conductor Electrode towards Ultrafast Na Storage

Haihua Wang (✉ whh@sust.edu.cn)

Shaanxi University of Science and Technology

Jing Zhang

Korea Univerisity

Jiliang Zhang

Korea Univerisity

Vincent Wing-hei Lau

Korea Univerisity

Gi-Hyeok Lee

Dongguk University

Kai Zhang

Nankai University

Mihui Park

Dongguk University

Liang Fang

Dongguk University

Yong-Mook Kang

Korea Univerisity

Physical Sciences - Article

Keywords: Prussian Blue, Fast kinetics, Job-sharing charge storage, Interfacial storage, Na rechargeable batteries

Posted Date: November 30th, 2020

DOI: <https://doi.org/10.21203/rs.3.rs-94792/v2>

License:  This work is licensed under a Creative Commons Attribution 4.0 International License.

[Read Full License](#)

1 **Job-Sharing Charge Storage in a Mixed Ion/Electron Conductor Electrode towards**
2 **Ultrafast Na Storage**

3 Jing Zhang¹, Jiliang Zhang¹, Vincent Wing-hei Lau¹, Haihua Wang^{2*}, Gi-Hyeok Lee³, Kai Zhang⁴,
4 Mihui Park³, Liang Fang³, and Yong-Mook Kang^{1*}

5 ¹Department of Materials Science and Engineering, Korea University, Seoul 02841, Republic of Korea

6 ²College of Chemistry and Chemical Engineering, Shaanxi University of Science and Technology, Xi'an,
7 710021, PR China

8 ³Department of Energy and Materials Engineering, Dongguk University-Seoul, Seoul 04620, Republic of
9 Korea

10 ⁴Key Laboratory of Advanced Energy Materials Chemistry (Ministry of Education), Renewable Energy
11 Conversion and Storage Center, College of Chemistry, Nankai University, Tianjin 300071, China

12 E-mail: dake1234@korea.ac.kr (Y.-M. Kang), whh@sust.edu.cn (H. Wang)

13 *KEYWORDS: Prussian Blue, Fast kinetics, Job-sharing charge storage, Interfacial storage, Na*
14 *rechargeable batteries*

15

16 For the cathode materials potentially available for high power capability, reducing their particle size can
17 improve the bulk ionic conductivity due to reduced ion diffusion length, and exploiting new reaction
18 mechanism must be fundamentally advantageous. However, other issues such as synthesis difficulty, poor
19 charge storage stability, and capacity decay can emerge. To simultaneously address these issues, in this
20 work, we first find solid-solid interfacial storage for the ultrafine insertion cathode materials in the space-
21 charge region of a mixed ion/electron conductor through the so-called “job-sharing” mechanism. This

22 mechanism shows that electrons and ions can be stored in the different phases around the interface and
23 transport only inside there, which looks thermodynamically distinct from most of conventional charge
24 storage mechanisms in terms of the relationship between charge storage and cell voltage. The insertion
25 cathodes governed by the “job-sharing” mechanism thus exhibit the outstanding performances with high
26 capacity, fast kinetics, and stable cyclability. Herein, the inverse conceptual compositing between ionic
27 conductor and electronic conductor to harness the size effect offers a potential research direction for not
28 only electrode design in high-power batteries, but also other electrochemical potential applications such
29 as solid-state electrolytes and so on.

30

31 Reversible electrochemical systems integrating high energy secondary battery and high power capacitor
32 look ideal, as they can simultaneously meet various demands of mobile electronic devices toward the use
33 for a longer time as well as electric vehicles toward a wider driving range and higher power capability.
34 The demand must be more challenging for sodium ion batteries (SIBs) due to the bigger size of Na^+ ion
35 (102 pm) than that of Li^+ ion (76 pm). A simple and straightforward approach to render secondary batteries
36 to be governed by faster kinetics for higher power capability is to reduce the particle size of electrode
37 materials to minimize the distance for ion transfer.¹ Particle miniaturization offers a high surface-to-
38 volume ratio, thereby exposing more surface sites as opposed to bulk ones. The surface atoms generally
39 have higher Gibbs free energy and more plentiful defects than its bulk homologue. Hence, the size
40 confinement effect in electrode materials is not limited to shortened ion transfer pathways but can also
41 induce unexpectedly rapid movement of electrons and ions in the enlarged space charge region which
42 may stem from higher contents of surface atoms.² Many unique physicochemical characteristics are
43 manifested in size-confined electrode materials, such as the variation of lattice parameter(s),³⁻⁵ chemical
44 potential,^{6,7} and electronic structure,⁸ all of which can affect their electrochemical behaviors. As for the

45 cathode materials, downsizing is reported to narrow the miscibility gap for phase transitions, facilitating
46 solid solution reactions for improved cyclic stability and reaction kinetics.⁹ Moreover, the solid solution
47 reaction facilitated by the size confinement can be typically found in some cathode materials like LiFePO_4
48 and LiMn_2O_4 because of the enhanced Li solubility in their nanocrystalline homologues.^{10,11} However,
49 the downsizing strategy is rarely reported for cathode materials, and in many cases, the size confinement
50 with cathode materials often results in the significant decrease of their capacities due to the breakage of
51 internal insertion sites in their crystal structures and the following reduction of inserted ions.³ Hence,
52 accentuating the merits of size confinement with cathode materials and mitigating its demerits are worth
53 being explored for innovating the cathode materials for alkali ion secondary batteries.

54 Novel mechanism for cathode materials should be developed and exploited to innovate the state-of-the-
55 art battery technologies. Adjusting the crystal structures of cathode materials can modulate the reaction
56 mechanism toward alkali ions, resultantly improving their energy densities, reversibility, and kinetics.¹²⁻
57 ¹⁵ The introduction of reversible Mn(II)/Mn(IV) redox couple can greatly increase the capacity of lithium-
58 excess Mn-based cathode.¹³ Putting hetero-species like crystal water and so on into a layered structure
59 (birnessite) cathode exploited the unprecedentedly reversible phase transition between the layered and a
60 metastable spinel-like structure for higher capacity as well as better cyclic stability.¹⁴ However, the
61 number of cathode materials governed by these new mechanisms is few, and so the brand-new mechanism
62 which can be generally applied for a lot of cathode materials is urgently required. Recently, a new
63 interfacial storage mechanism named job-sharing storage which differs from conventional reaction
64 mechanisms like intercalation, conversion, etc. has been proposed by Maier et al.^{7,16-19} This mechanism
65 reveals that positive and negative charges can be stored separately in two different phases within
66 nanocomposites, contributing additional capacity independent of bulk storage. The reaction kinetics could
67 be ultrafast because the transfer of two charge carriers is also independent. The job-sharing storage was

68 reported to primarily govern the reaction kinetics of transition metal oxides which depend on conversion
69 reaction. However, this mechanism has never been demonstrated in the electrode materials with other
70 reaction mechanisms such as intercalation and so on. Because the job-sharing storage is limited in the
71 space-charge region and thus the following capacity and kinetics are determined by the ratio of boundary
72 region, its universal extension to intercalation and so forth could be accelerated by our size confinement
73 strategy with cathode materials.

74 Herein, for the first time, we report the application of this brand-new job-sharing mechanism for size-
75 confined insertion-type cathode materials to achieve a high energy, high power, and highly stable battery.
76 We selected Prussian blue analogues (PBAs), one of the commonly used cathodes for SIBs, as a proof of
77 concept to fabricate an artificial mixed conductor by compositing iron hexacyanoferrate nanodots (FeHCF
78 NDs) as an ionic conductor with reduced graphene oxide (rGO) as an electron conductor. This composite
79 was synthesized by a two-step ion-exchange method with FeOOH NDs/rGO composite as a precursor
80 (Fig. 1a, Supplementary Fig. 1–3). The strong interaction between FeHCF NDs and rGO enables the ion
81 and electron pathway to be decoupled within the space-charge region of this composite. The job-sharing
82 mechanism was well clarified, which is totally different from the traditional charge storage mechanisms
83 such as intercalation, conversion and so on. The capacity-voltage relation of interfacial storage in the three
84 modes is updated against that of the bulk one. The FeHCF NDs/rGO composite thus shows beneficial
85 interface/surface behavior and excellent electrochemical performance. Therefore, the mixed electron/ion
86 conductor, FeHCF NDs/rGO, paves a novel way for the charge storage for alkali ion secondary batteries.

87 **Material characterizations**

88 Field emission scanning electron microscopy (FESEM), transmission electron microscope (TEM), and
89 high-resolution TEM (HRTEM) images of FeHCF NDs/rGO (Fig. 1b–e, Supplementary Fig. 4) show that
90 the ultrafine nanodots are tightly and uniformly embedded into the graphene sheets with a monodisperse

91 feature and a homogeneous distribution of Na, Fe, C, and N (Supplementary Fig. 5). The lattice fringes
92 with a d-spacing of 0.258 nm correspond to the (400) plane of FeHCF. The nanodots have an average size
93 of 9.7 nm (Fig. 1f), which is one of the smallest particle sizes of high-quality PBAs in the consensus
94 reports. For comparison, a poorly contacted FeHCF microcubes/rGO composite (FeHCF MCs/rGO;
95 Supplementary Fig. 6) with particle size up to submicron (~ 293 nm) was formed when higher ascorbic
96 acid amount (50 mg) was used (2 mg for FeHCF NDs/rGO), resulting in a much lower specific surface
97 area ($57.6 \text{ m}^2 \text{ g}^{-1}$) than FeHCF NDs/rGO ($148 \text{ m}^2 \text{ g}^{-1}$) (Supplementary Fig. 7).

98 The formula (Supplementary Fig. 8, Supplementary Table 1) of FeHCF MCs/rGO and FeHCF
99 NDs/rGO are quantified to be $\text{Na}_{0.89}\text{FeFe}(\text{CN})_6 \cdot 1.86\text{H}_2\text{O}$ and $\text{Na}_{0.96}\text{FeFe}(\text{CN})_6 \cdot 2.09\text{H}_2\text{O}$, respectively.
100 The powder X-ray diffraction (XRD) patterns (Fig. 2a) of the two samples are indexed to the face-
101 centered-cubic structure (space group $Fm\bar{3}m$), which agrees well with previous reports.^{20,21} The broad
102 peaks of FeHCF NDs/rGO are attributed to its small size. The calculated lattice parameter of FeHCF
103 NDs/rGO ($a = 10.255 \text{ \AA}$) is larger than that of FeHCF MCs/rGO ($a_0 = 10.221 \text{ \AA}$), revealing the lattice
104 expansion of ultrafine crystals (Supplementary Table 2, Supplementary Note 1). The size-dependent
105 lattice expansion has been found in a lot of materials, such as LiCoO_2 , CeO_2 , TiO_2 (rutile), BaTiO_3 ,
106 MnCr_2O_4 , ZnO , Ni , and MgO .^{3,22-24} The different features of Fe K-edge X-ray absorption near-edge
107 structure (XANES) spectra (Fig. 2b, Supplementary Note 2) for the two samples are attributed to the high
108 surface atom ratio and the low crystallinity of size-confined sample that cause the different types of ligand
109 bonded with the Fe atoms at the surface. The poor symmetry of the related extended X-ray absorption
110 fine structure (EXAFS) spectrum (Fig. 2c) reveals the distortion of the structure for FeHCF ND compared
111 with FeHCF MCs.²⁵

112 The Raman spectrum (Fig. 2d, Supplementary Note 3) of FeHCF NDs/rGO shows a significant
113 reduction of intensity for the C \equiv N vibration compared with that of FeHCF MCs/rGO, suggesting that the
114 shrinkage of the long-range structure suppresses the vibrational stretching mode of the ultrafine
115 particles.²⁶ Besides, size-induced frequency shift to lower wavenumber is observed (Supplementary Table
116 2), which is partially caused by the increase of bond distance resulting from lattice expansion and may
117 partly be due to the phonon confinement effect within the small sized grains.^{3,27} A peak shift to lower
118 binding energy is observed in the Fe 2p X-ray photoelectron spectroscopy (XPS) spectra (Fig. 2e,
119 Supplementary Table 2, Supplementary Note 3) of FeHCF NDs/rGO, revealing Fe in Prussian blue
120 attracts electrons from the π - π conjugated system of graphene.²⁸ It further indicates the interaction within
121 the close contact interface of the composite. Similar conclusion can be drawn from N 1s spectra (Fig. 2f)
122 that show an increase in relative peak intensities of N(399.8 eV) and N(402.4 eV) to N(397.7 eV) for
123 FeHCF NDs/rGO. In short, the ultrafine FeHCF nanocrystallines show expanded lattice, low degree of
124 order, high structural distortion, and intense interaction with graphene layers.

125 **Electrochemical behavior**

126 Both the cyclic voltammograms (CV) and galvanostatic charge/discharge profiles (Fig. 3a, c) of FeHCF
127 MCs/rGO have the typical profile of bulk sodium iron hexacyanoferrates with two redox couples
128 (Supplementary Note 4). After downsizing, they show a different characteristic with weakened peaks and
129 platforms (Fig. 3b, d). Both of the curves show enhanced capacity in the lower voltage region. The
130 contraction of the miscibility gap that makes the charge/discharge curves of FeHCF NDs/rGO smoother
131 (Fig. 3d) suggests that the thermodynamics and kinetics associated with phase-transition in size-confined
132 particles are different from those in bulk-sized particles.²⁹ This phenomenon appears in many size
133 confinement systems.^{3,9,10,30}

134 Now we take the mixed conductor into account and focus on the interface between FeHCF and rGO in
135 the space-charge zone. Electroneutrality is governed by Poisson-Boltzmann's equation which depends on
136 the difference in structure and electrical potential at the interface and in the bulk.¹⁷ As a result, the charge
137 carriers (including electron and ion) are re-distributed and can be considered independently at the interface
138 (but are coupled in the bulk).³¹ A contour map (Fig. 3e) of charge carrier concentration derived from
139 Gouy-Chapman profiles shows the redistribution of charge carriers at the FeHCF NDs/rGO interface,
140 indicating mutative charge storage from bulk to interface. In this case, the charge storage in the interface
141 complies with a job-sharing mechanism illustrated in Fig. 3f, which suggests that the ions (e.g., Na⁺) can
142 store and transport in one phase (e.g., PB) and electrons in the other phase (e.g., graphene) within the two-
143 phase interface. This storage is heavily dependent on size effect and two-phase contacts. The relationship
144 between charge Q stored in the space-charge zone and the particle thickness l (Supplementary Fig. 9)
145 illustrates how Q increases in nanoscale materials and even more so for atomic-scale size.⁷ In our case,
146 the space-charge zone covers a large part of the FeHCF ND particle. Both the contact area and space-
147 charge zone of FeHCF NDs/rGO are much larger than those of FeHCF MCs/rGO. Therefore, interfacial
148 storage contributes or even dominates the mass storage mechanism for the ND composite, but is negligible
149 for FeHCF MCs/rGO. Experimental verification (Supplementary Fig. 10) suggests that the capacity of
150 the composite is not just provided by the single phase FeHCF NDs or rGO; more importantly, the
151 interfacial storage also makes a great contribution to the total capacity of the composite.

152 For simplicity (ignoring intrinsic contribution), the thermodynamic description of the relationship
153 between Na activity a_{Na} and job-sharing stored charge Q is given via $a_{\text{Na}} \propto Q^n \exp(kQ)$ (calculation cf.
154 ref.¹⁷), where n is between 3 and 4, depending on the condition of contact phases, and k is a constant. Note
155 that this equation represents the capacity-voltage relation according to $E = \text{const.} - (RT/F) \ln a_{\text{Na}}$. In the
156 bulk, however, the relation follows $a_{\text{Na}} \propto Q^2$. The differences are shown in the illustration of the $\ln a_{\text{Na}}$ -

157 Q profiles (Supplementary Fig. 11). The job-sharing storage contains three modes as given by (for more
158 details, see Methods): (i) intrinsic characteristics ($a_{\text{Na}} = \text{const.}$); (ii) diffusive-layer ($a_{\text{Na}} \propto Q^n$); and (iii)
159 rigid-layer ($a_{\text{Na}} \propto \exp(kQ)$). To reveal the correlation, we fitted $\ln Q$ vs. E plots (Fig. 3g) derived from
160 the discharge curve of FeHCF NDs/rGO at different voltages (Supplementary Fig. 12). The power-law
161 exponent n only at a high voltage range of 3.5–3.9 V is between 3 and 4, indicating the charge storage
162 dominated by a diffuse layer. The power-law function demonstrates an irrational fit ($n < 3$) when voltage
163 is lower than 3.5 V. To reveal the effect of a rigid layer, we plotted $E + nRT \ln Q/F$ vs. Q with $n = 3$ and 4,
164 respectively (Fig. 3h).³² The plots reveal a linear correlation when $Q > 60 \text{ mAh g}^{-1}$ with a k value of 0.01
165 for both $n = 3$ and 4. The job-sharing storage is overall based on the rigid-layer mode that is applicable in
166 a wide voltage range, consistent with extra capacity observed in the CV and charge/discharge curves. In
167 this regime, the storage shows a capacitor-like behavior that functions in the solid/solid interface.

168 One advantage of the job-sharing effect is to provide extra capacity. The insertion capacity of ion
169 insertion type framework is decreasing with the reduction of particle size. The insertion capacity of
170 FeHCF loses nearly 20 mAh g^{-1} from bulk to a $10\text{nm} \times 10\text{nm} \times 10\text{nm}$ cube (Methods, Supplementary Fig.
171 13, Fig. 3i). However, the two samples show the same capacity at 0.2 C, which is credited to the high
172 interface storage as mentioned above.

173 **Electrochemical reaction kinetics**

174 Mass transfer in the mixed ion/electron conductor could be very fast due to the size confinement effect
175 and the job-sharing mechanism. This is confirmed by the superior rate ability (Fig. 4a) of FeHCF
176 NDs/rGO. The charge-discharge curves of FeHCF NDs/rGO (Fig. 4b) at various current densities (0.2 C
177 to 50 C) display similar curve shape, while those of FeHCF MCs/rGO (Fig. 4c) appear to have obvious
178 polarization at high C-rates. Furthermore, FeHCF MCs/rGO shows higher overpotential at high rates,

179 leading to a higher voltage hysteresis (Supplementary Fig. 14), which are indicative of reduced kinetics
180 and energy efficiency.³³ For comparison, the rate capability of FeHCF NDs/rGO (Fig. 4d) is superior to
181 other state-of-the-art PBA-based cathodes,^{25,34-41} especially at high current densities.

182 To account for the superior rate capability of FeHCF NDs/rGO, we employed several methodologies
183 to investigate the origin of the outstanding electrochemical reaction kinetics. The difference of the
184 calculated b -values (Methods, Supplementary Fig. 15a, b, Fig. 4e) indicates both diffusion-controlled and
185 capacitive processes in the Na storage mechanism of FeHCF NDs/rGO, of which the latter dominates,³⁰
186 while Na storage for FeHCF MCs/rGO is largely diffusion-controlled at a low scan rate but is more
187 capacitive with increasing scan rate. Note that this capacitive behavior includes common
188 pseudocapacitance and interfacial storage, and both of them result in fast charge/discharge. However,
189 according to previous publications reporting that size reduction of the cathode material in and of itself
190 leads to lower capacity,^{3,42} we believe the extra capacity in FeHCF NDs/rGO is mostly contributed by
191 interfacial storage. The calculated surface/interface contribution ratios (Methods, Fig. 4f, Supplementary
192 Fig. 15c) of the two electrodes show the same conclusion as the b -value. Note that, at a high rate,
193 diffusivity is the bottleneck to capacity contribution of FeHCF MCs/rGO.

194 Analysis of ion diffusion kinetics helps understand this. Size confinement effect and space-charge effect
195 jointly are factors to ultra-fast kinetics. Generally speaking, ion diffusion is the rate-determining step for
196 the electrochemical reaction. The diffusion time (τ^δ) is proportional to L^2/D^δ , where L is the diffusion
197 length and D^δ is the diffusion coefficient,⁴³ so shortening L or increasing D^δ can promote the diffusion
198 kinetics. In our case, the L for FeHCF MCs is almost 30 times larger than that of FeHCF NDs on average,
199 meaning that the diffusion time of the former is almost 900 times higher than that of the latter, assuming
200 an identical D^δ in both cases. On the other hand, diffusion time τ^δ also refers to transport resistance R^δ and
201 chemical capacitance C^δ by the expression $\tau^\delta = R^\delta C^\delta$.¹⁸ Hence D^δ is influenced by the two terms, $1/R^\delta$ and

202 $1/C^\delta$, when L is fixed. D^δ is expressed differently for bulks and interfaces (Supplementary Table 3). By
203 inspecting these expressions, two aspects are evident that can rationalize why $D_{\text{interface}}$ is greater than
204 D_{bulk} .^{18,19} (i) In bulk materials, the ions and electrons are transferred along the same pathway, whereas in
205 the job-sharing interface, they are decoupled and are transported within their respective conductor (Fig.
206 3f), leading to a low resistance R^δ . (ii) For the job-sharing mode, there is an extra term $(\frac{F^2 s^2}{RT \epsilon \epsilon_0})$ related to
207 the electrostatic energy in $1/C^\delta$ that reduces the capacitance term C^δ .

208 The Na ion diffusion coefficient D_{Na} ($\text{cm}^2 \text{s}^{-1}$) can be calculated via the galvanostatic intermittent
209 titration technique (GITT) (Methods, Supplementary Fig. 16, Fig. 4g).^{44,45} FeHCF NDs/rGO overall
210 shows a higher D_{Na} value (10^{-8} to $10^{-11} \text{cm}^2 \text{s}^{-1}$) compared with FeHCF MCs/rGO (10^{-10} to $10^{-13} \text{cm}^2 \text{s}^{-1}$)
211 over both charging and discharging, and is higher than those of many other PBA-based cathodes as
212 well.^{40,46} To sum up, the combination of the small diffusion length and the high diffusion coefficient lead
213 to the fast ion diffusion kinetics of FeHCF NDs/rGO electrode, which removes the solid-state diffusion
214 as a limiting factor and makes the surface/interface storage the dominant contributor to capacity. For
215 FeHCF MCs/rGO, however, the longer diffusion path and the low diffusion coefficient for Na ions induce
216 a diffusion-controlled process at low C-rate. At high current density, which requires short reaction time,
217 Na ions probably only diffuse over a short-distance and occupy near-surface reaction sites within FeHCF
218 MCs/rGO (Supplementary Fig. 17). Ex-situ XPS analyses (Supplementary Fig. 18, Fig. 4h,
219 Supplementary Table 4) confirm that Na ions are only inserted into the near-surface sites of FeHCF MCs
220 at high C-rate. Besides, a lower charge transfer resistance (R_{ct}) and a higher diffusion coefficient obtained
221 from electrochemical impedance spectroscopy (EIS) (Supplementary Fig. 19) confirm the superiority of
222 the size-confined sample further.

223 Fig. 4i shows schematic graphical summary of the kinetic mechanism where the interface, surface, and
224 crystal interior act in concert for charge storage. The extensive contact of the two conductors and highly
225 exposed surfaces contribute to high interfacial (solid-solid contact) and surface (solid-electrolyte contact)
226 storage. This charge storage mechanism shows an excellent kinetic characteristic. The job-sharing
227 transport ensures the high conductivity of both electrons and ions that allow fast Na^+ diffusion in the
228 internal structure owing to the much more shortened ion diffusion length.

229 **Electrochemical reaction stability**

230 Fig. 5a shows the capacity retention upon cycling for the two electrodes. An outstanding cyclability of
231 FeHCF NDs/rGO is observed, showing a capacity of 128 mAh g^{-1} over 100 cycles with only 3% capacity
232 loss. However, for FeHCF MCs/rGO, the capacity decreases to 102 mAh g^{-1} after 100 cycles with a
233 capacity retention of 77.9%. The high stability of FeHCF NDs/rGO is also confirmed by the stable
234 Coulombic efficiency (CE), the value of which stabilizes to 99.5+% after 8 cycles. In contrast, the CE of
235 FeHCF MCs/rGO is more erratic after 26 cycles, and swings between 97.5% and 101.4%. The superb
236 structural stability of the FeHCF NDs/rGO was further verified by cycling at 10 C (Fig. 5b), showing a
237 high capacity changing from 104 mAh g^{-1} to 84 mAh g^{-1} over 1000 cycles with a high and stable CE of
238 99+%. The full cell test (Supplementary Fig. 20, 21) with a good electrochemical performance suggests
239 the practical applicability of FeHCF NDs/rGO sample for high-energy and high-power batteries.

240 Ex-situ XRD over one complete cycle was used to explore the structure change (Supplementary Note
241 5). The structures of both electrodes (Fig. 5d, h) reversibly evolve between rhombohedral (R) phase
242 ($\text{Na}_2\text{Fe}^{\text{II}}\text{Fe}^{\text{II}}(\text{CN})_6$) and cubic (C) phase ($\text{Fe}^{\text{III}}\text{Fe}^{\text{III}}(\text{CN})_6$).²¹ However, FeHCF NDs/rGO shows a smaller
243 shift during charging/discharging (Fig. 5e, i, Supplementary Fig. 22), indicating a smaller lattice variation
244 as compared with FeHCF MCs/rGO. Moreover, a small unit cell volume variation of below 2.4% is for
245 FeHCF NDs/rGO, indicative of a highly reversible phase transition, whereas that is 4.4% for FeHCF

246 MCs/rGO (Fig. 5f, j). The excellent cyclability of FeHCF NDs/rGO can be attributed to the small
247 structural distortion during sodiation/desodiation. The inherent features of ultrafine PB nanocrystals,
248 including a larger lattice, low degree of order, and low structural symmetry, are the most significant
249 contributor to restraining the lattice distortion upon charge/discharge.

250 In summary, we implement the first case of job-sharing storage for the insertion-type cathode materials
251 through the formation of an artificial mixed ion/electron conductor. The job-sharing mechanism, coupled
252 with the size confinement effect, displays several benefits: (1) an additional capacity contribution to
253 compensate for the insertion capacity decrease associated with particle downsizing; (2) the short ion
254 diffusion length and job-sharing transport of ions and electrons lead to outstanding mass transport in the
255 space-charge zone, thereby yielding superb capacities at high C-rates; (3) the lattice expansion and
256 distortion in the size-confined particles limit the structural variation of FeHCF NDs/rGO during Na⁺ ions
257 insertion/extraction, allowing an ultra-stable cyclability. This finding is significant since it is widely
258 applicable to develop insertion-type cathode system of alkali ion secondary batteries. Our work regarding
259 the use of size effect and space-charge effect suggests a new and universal strategy for high-power
260 batteries and also other fields.

261

262 1 Jung, S.-K. et al. Nanoscale phenomena in lithium-ion batteries. *Chem. Rev.* **120**, 6684–6737 (2020).

263 2 Maier, J. Pushing nanoionics to the limits: charge carrier chemistry in extremely small systems. *Chem.*
264 *Mater.* **26**, 348-360 (2014).

265 3 Okubo, M. et al. Nanosize effect on high-rate Li-ion intercalation in LiCoO₂ electrode. *J. Am. Chem. Soc.*
266 **129**, 7444-7452 (2007).

267 4 Perebeinos, V., Chan, S.-W. & Zhang, F. ‘Madelung model’ prediction for dependence of lattice parameter
268 on nanocrystal size. *Solid State Commun.* **123**, 295-297 (2002).

269 5 Diehm, P. M., Ágoston, P. & Albe, K. Size-dependent lattice expansion in nanoparticles: reality or anomaly?
270 *ChemPhysChem* **13**, 2443-2454 (2012).

271 6 Jamnik, J. & Maier, J. Nanocrystallinity effects in lithium battery materials aspects of nano-ionics. Part IV.
272 *Phys. Chem. Chem. Phys.* **5**, 5215-5220 (2003).

273 7 Maier, J. Thermodynamics of electrochemical lithium storage. *Angew. Chem. Int. Ed.* **52**, 4998-5026
274 (2013).

275 8 Qian, D. et al. Electronic spin transition in nanosize stoichiometric lithium cobalt oxide. *J. Am. Chem. Soc.*
276 **134**, 6096-6099 (2012).

277 9 Wang, B. et al. LiFePO₄ quantum-dots composite synthesized by a general microreactor strategy for ultra-
278 high-rate lithium ion batteries. *Nano Energy* **42**, 363-372 (2017).

279 10 Kobayashi, G. et al. Isolation of solid solution phases in size-controlled Li_xFePO₄ at room temperature.
280 *Adv. Funct. Mater.* **19**, 395-403 (2009).

281 11 Okubo, M. et al. Fast Li-ion insertion into nanosized LiMn₂O₄ without domain boundaries. *ACS Nano* **4**,
282 741-752 (2010).

283 12 Eum, D. et al. Voltage decay and redox asymmetry mitigation by reversible cation migration in lithium-
284 rich layered oxide electrodes. *Nat. Mater.* **19**, 419-427 (2020).

285 13 Lee, J. et al. Reversible Mn²⁺/Mn⁴⁺ double redox in lithium-excess cathode materials. *Nature* **556**, 185-190
286 (2018).

287 14 Jo, M. R. et al. Triggered reversible phase transformation between layered and spinel structure in
288 manganese-based layered compounds. *Nat. Commun.* **10**, 3385 (2019).

289 15 Wang, F. et al. Ternary metal fluorides as high-energy cathodes with low cycling hysteresis. *Nat. Commun.*
290 **6**, 6668 (2015).

291 16 Chen, C.-C. & Maier, J. Decoupling electron and ion storage and the path from interfacial storage to
292 artificial electrodes. *Nat. Energy* **3**, 102-108 (2018).

293 17 Chen, C. C. & Maier, J. Space charge storage in composites: thermodynamics. *Phys. Chem. Chem. Phys.*
294 **19**, 6379-6396 (2017).

295 18 Chen, C.-C., Navickas, E., Fleig, J. & Maier, J. Kinetics of space charge storage in composites. *Adv. Funct.*
296 *Mater.* **28**, 1705999 (2018).

297 19 Chen, C. C., Fu, L. & Maier, J. Synergistic, ultrafast mass storage and removal in artificial mixed
298 conductors. *Nature* **536**, 159-164 (2016).

299 20 Li, W.-J. et al. Facile method to synthesize Na-enriched Na_{1+x}FeFe(CN)₆ frameworks as cathode with
300 superior electrochemical performance for sodium-ion batteries. *Chem. Mater.* **27**, 1997-2003 (2015).

301 21 You, Y., Wu, X.-L., Yin, Y.-X. & Guo, Y.-G. High-quality Prussian blue crystals as superior cathode
302 materials for room-temperature sodium-ion batteries. *Energy Environ. Sci.* **7**, 1643-1647 (2014).

303 22 Tsunekawa, S. et al. Critical size and anomalous lattice expansion in nanocrystalline BaTiO₃ particles. *Phys.*
304 *Rev. B* **62**, 3065 (2000).

305 23 Bhowmik, R., Ranganathan, R. & Nagarajan, R. Lattice expansion and noncollinear to collinear
306 ferrimagnetic order in a MnCr₂O₄ nanoparticle. *Phys. Rev. B* **73**, 144413 (2006).

307 24 Ali, M. & Winterer, M. ZnO nanocrystals: surprisingly ‘alive’. *Chem. Mater.* **22**, 85-91 (2010).

308 25 Xie, B. et al. Achieving long-life Prussian blue analogue cathode for Na-ion batteries via triple-cation
309 lattice substitution and coordinated water capture. *Nano Energy* **61**, 201-210 (2019).

310 26 Toulouse, J., DiAntonio, P., Vugmeister, B., Wang, X. & Knauss, L. Precursor effects and ferroelectric
311 macroregions in KTa_{1-x}Nb_xO₃ and K_{1-y}Li_yTaO₃. *Phys. Rev. Lett.* **68**, 232 (1992).

- 312 27 Lin, T., Cong, X., Lin, M.-L., Liu, X.-L. & Tan, P.-H. The phonon confinement effect in two-dimensional
313 nanocrystals of black phosphorus with anisotropic phonon dispersions. *Nanoscale* **10**, 8704-8711 (2018).
- 314 28 Feng, J. X. et al. Silica-polypyrrole hybrids as high-performance metal-free electrocatalysts for the
315 hydrogen evolution reaction in neutral media. *Angew. Chem.* **56**, 8120-8124 (2017).
- 316 29 Wagemaker, M. et al. Dynamic solubility limits in nanosized olivine LiFePO₄. *J. Am. Chem. Soc.* **133**,
317 10222-10228 (2011).
- 318 30 Tang, Y. et al. Identifying the origin and contribution of surface storage in TiO₂(B) nanotube electrode by
319 in situ dynamic valence state monitoring. *Adv. Mater.* **30**, 1802200 (2018).
- 320 31 Maier, J. Nanoionics: ion transport and electrochemical storage in confined systems. *Nat. Mater.* **4**, 805-
321 815 (2005).
- 322 32 Fu, L., Chen, C. C., Samuelis, D. & Maier, J. Thermodynamics of lithium storage at abrupt junctions:
323 modeling and experimental evidence. *Phys. Rev. Lett.* **112**, 208301 (2014).
- 324 33 Ren, W. et al. Prussian white hierarchical nanotubes with surface-controlled charge storage for sodium-ion
325 batteries. *Adv. Funct. Mater.* **29**, 1806405 (2019).
- 326 34 Huang, Y. et al. A chemical precipitation method preparing hollow-core-shell heterostructures based on
327 the Prussian blue analogs as cathode for sodium-ion batteries. *Small* **14**, 1801246 (2018).
- 328 35 Zhang, W. et al. Synthesis of monocrystalline nanoframes of Prussian blue analogues by controlled
329 preferential etching. *Small* **55**, 8228-8234 (2016).
- 330 36 Li, L., Nie, P., Chen, Y. & Wang, J. Novel acetic acid induced Na-rich Prussian blue nanocubes with iron
331 defects as cathodes for sodium ion batteries. *J. Mater. Chem. A* **7**, 12134-12144 (2019).
- 332 37 Huang, Y. et al. A novel border-rich Prussian blue synthesized by inhibitor control as cathode for sodium
333 ion batteries. *Nano Energy* **39**, 273-283 (2017).
- 334 38 Li, W. et al. Remarkable enhancement in sodium-ion kinetics of NaFe₂(CN)₆ by chemical bonding with
335 graphene. *Small Methods* **2**, 1700346 (2018).
- 336 39 Fu, H. et al. Enhanced storage of sodium ions in Prussian blue cathode material through nickel doping. *J.*
337 *Mater. Chem. A* **5**, 9604-9610 (2017).
- 338 40 Li, W. et al. Stress distortion restraint to boost the sodium ion storage performance of a novel binary
339 hexacyanoferrate. *Adv. Energy Mater.* **10**, 1903006 (2020).
- 340 41 Peng, J. et al. A Dual-Insertion type sodium-ion full cell based on high-quality ternary-metal Prussian blue
341 analogs. *Adv. Energy Mater.* **8**, 1702856 (2018).
- 342 42 Lesel, B. K., Cook, J. B., Yan, Y., Lin, T. C. & Tolbert, S. H. Using nanoscale domain size to control
343 charge storage kinetics in pseudocapacitive nanoporous LiMn₂O₄ powders. *ACS Energy Lett.* **2**, 2293-2298
344 (2017).
- 345 43 Zhu, C., Usiskin, R. E., Yu, Y. & Maier, J. The nanoscale circuitry of battery electrodes. *Science* **358**,
346 ea02808 (2017).
- 347 44 Zhang, J. et al. Bifunctional conducting polymer coated CoP core-shell nanowires on carbon paper as a
348 free-standing anode for sodium ion batteries. *Adv. Energy Mater.* **8**, 1800283 (2018).
- 349 45 Zhang, J. et al. Engineering solid electrolyte interphase on red phosphorus for long-term and high-capacity
350 sodium storage. *Chem. Mater.* **32**, 448-458 (2020).
- 351 46 You, Y. et al. Subzero-temperature cathode for a sodium-ion battery. *Adv. Mater.* **28**, 7243-7248 (2016).
- 352
- 353

354 **Acknowledgements**

355 This work was supported by the National Research Foundation of Korea (NRF) grant funded by the Korea
356 government (MSIP) under “Middle Career Program” (NRF-2017R1A2B3004383), “Science Research
357 Centre” (NRF-2017R1A5A1015365), and “Creative Materials Discovery Program” (NRF-
358 2017M3D1A1039553).

359 **Author contributions**

360 Jin.Z. and Y.-M.K. designed the project. Jin.Z. synthesized and characterized the materials and performed
361 the electrochemistry experiments. Jil.Z., G.-H.L. and L.F. performed synchrotron-based measurements
362 and analysed the data. Jin.Z. and M.P. performed TEM, Raman and XPS tests. V.W.L., H.W. and K.Z.
363 offered valuable comments for this project. All authors discussed and analysed the data. Jin.Z., H.W. and
364 Y.-M.K. wrote the manuscript with input from all co-authors.

365 **Competing interests**

366 The authors declare no competing interests.

367 **Data availability**

368 Any source data are available at <https://pan.baidu.com/s/1sjUDZgdLi0jWWor7zbnkZg>.

369 **Code availability**

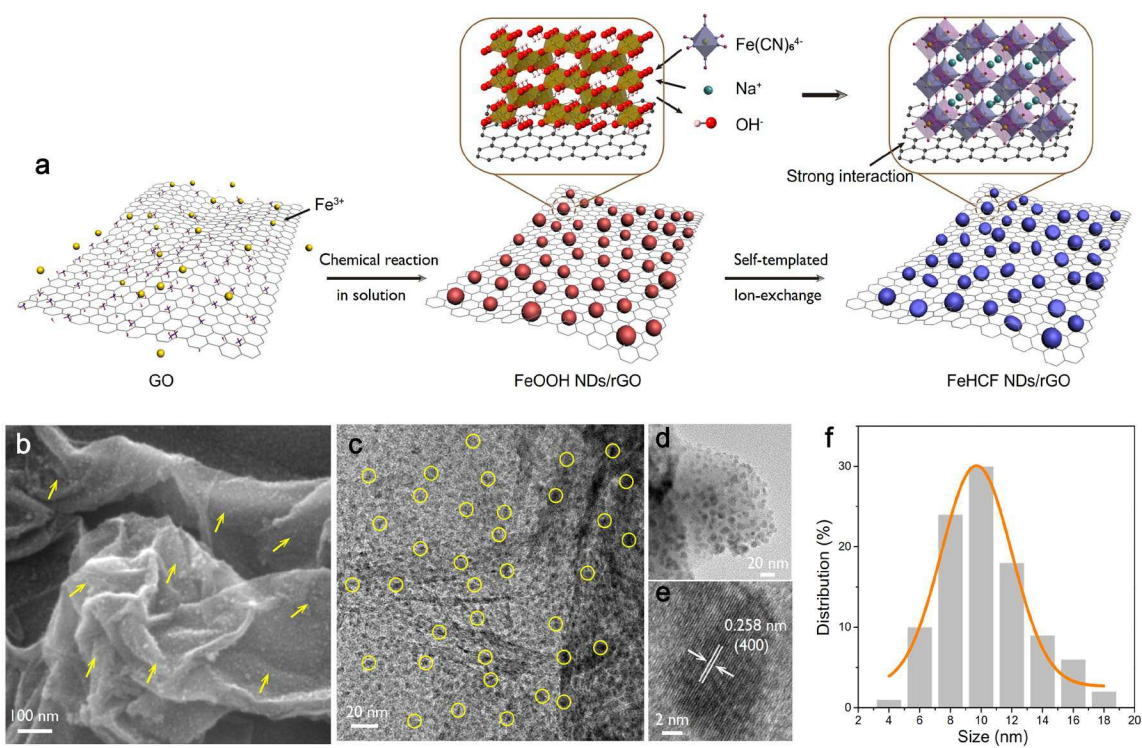
370 The accession code is publicly available at
371 <https://drive.google.com/drive/folders/1nGOcVMJMuWDgBmjOiZlhzvafnmDu8HUy?usp=sharing>

372 **Additional information**

373 **Supplementary information** is available for this paper at www.nature.com/nature.

374 **Correspondence and requests for materials** should be addressed to Y.-M. Kang and H. Wang

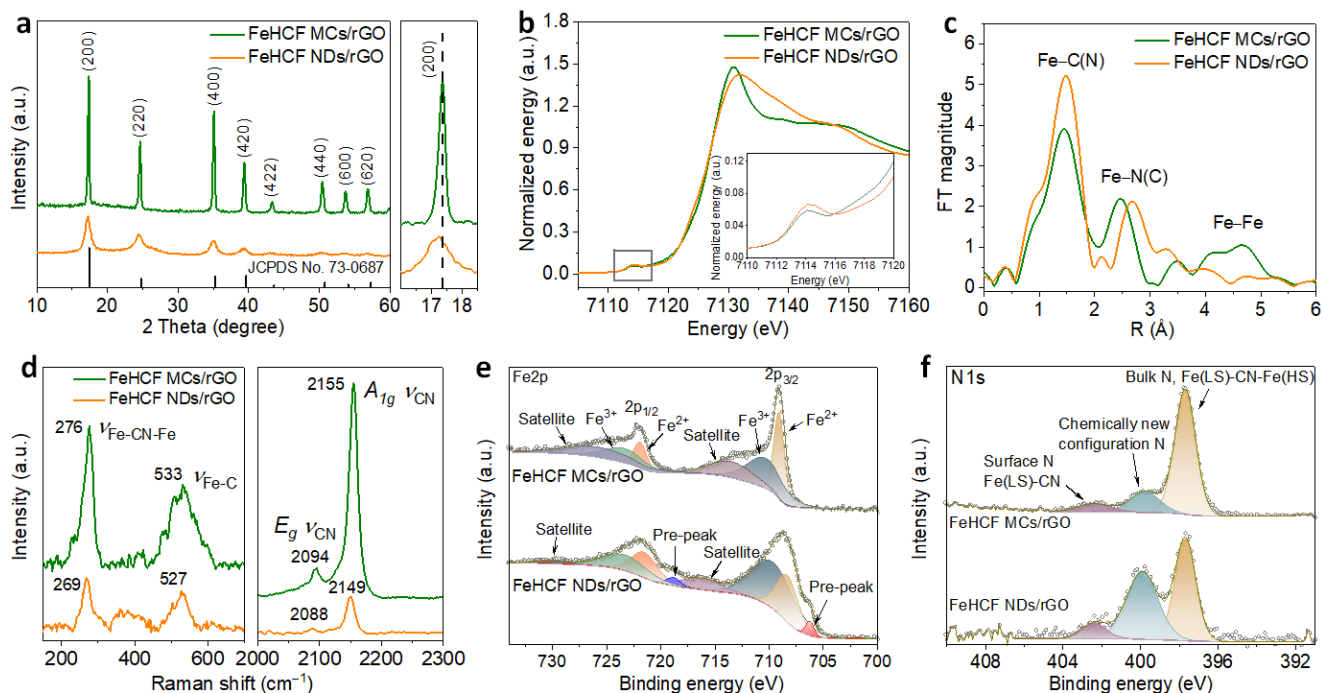
375



377

378 **Fig. 1 Synthesis process and microstructural analyses of FeHCF NDs/rGO.** **a**, Schematic illustration
 379 of the synthesis process by a two-step method. **b**, SEM image. **c**, **d**, TEM images. **e**) HRTEM image. **f**,
 380 Particle size distribution of FeHCF NDs (200 particles counted).

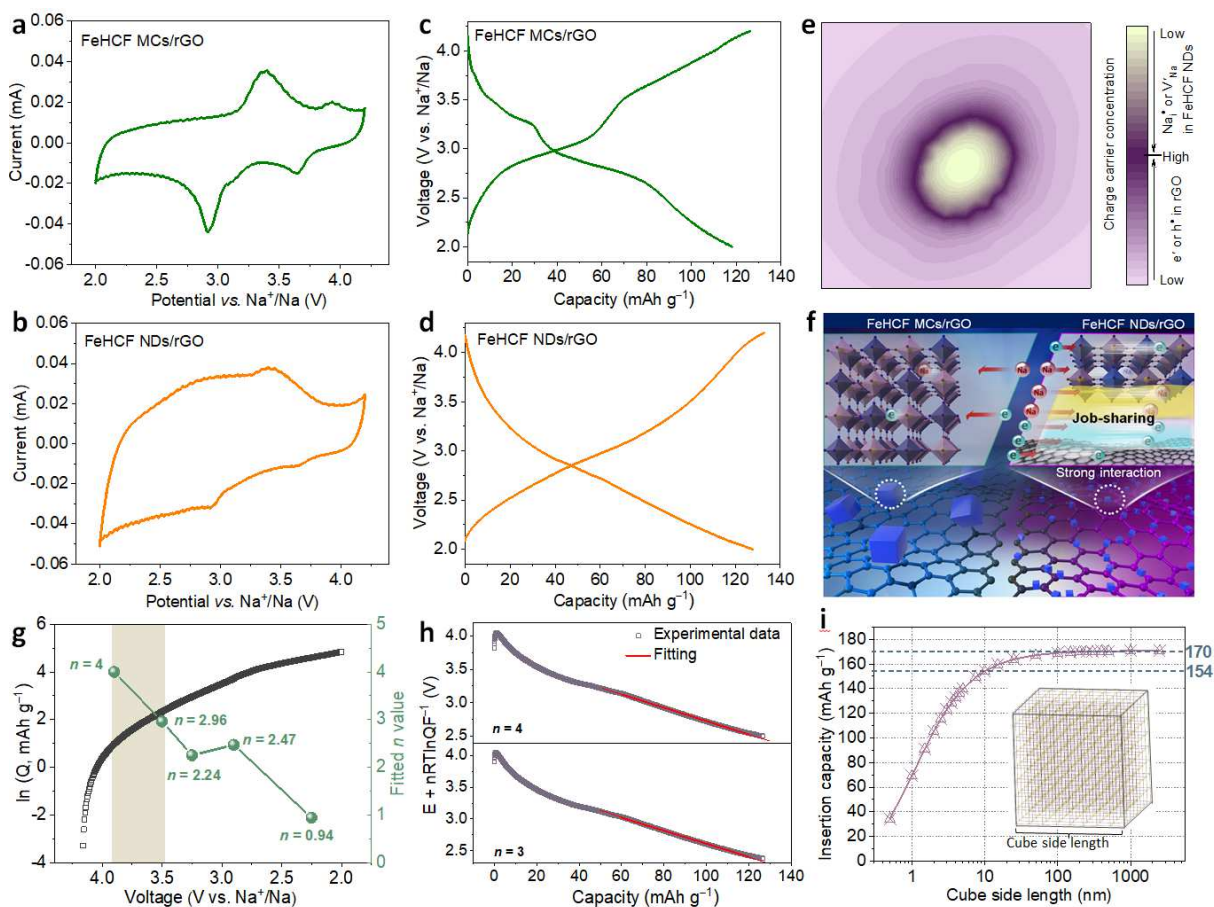
381



382

383 **Fig. 2 Structure characterizations of FeHCF MCs/rGO and FeHCF NDs/rGO.** **a**, XRD patterns,
 384 including an enlargement of the region around the (200) reflection. **b**, XANES spectra of the Fe K-edge;
 385 inset shows the expanded pre-edge region. **c**, Fourier transformed EXAFS spectra of the Fe K-edge. **d**,
 386 Raman spectra. **e**, Fe 2p XPS spectra. **f**, N 1s XPS spectra.

387

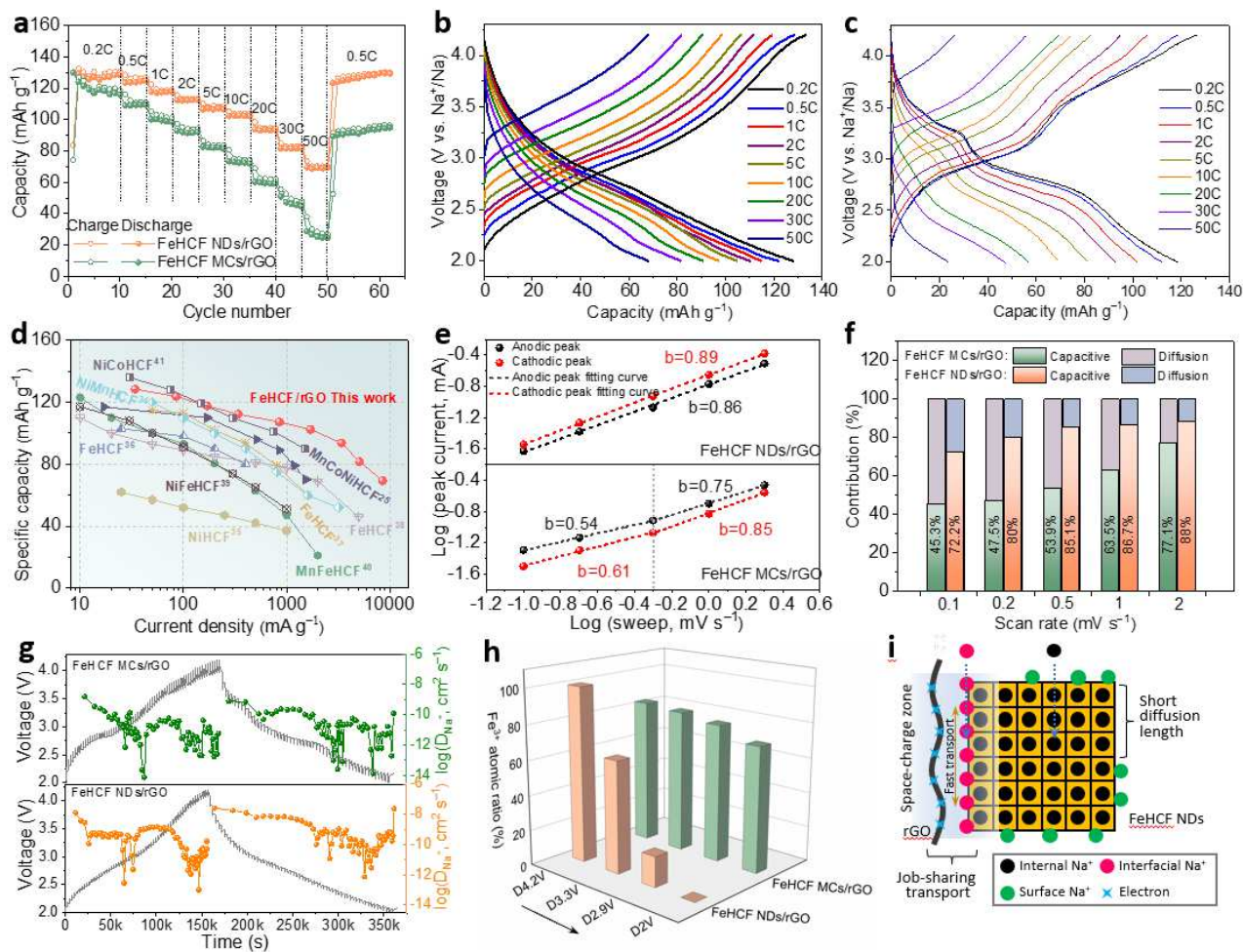


388

389 **Fig. 3 General electrochemical analyses.** Typical CV curves at 0.1 mV s⁻¹ of **a** FeHCF MCs/rGO and **b**
 390 FeHCF NDs/rGO. Typical galvanostatic charge/discharge profiles at 0.2 C (1 C = 170 mA g⁻¹) of **c** FeHCF
 391 MCs/rGO and **d** FeHCF NDs/rGO. **e**, Visible redistribution of charge carriers at the FeHCF NDs/rGO
 392 interface. Na⁺ interstitials Na_i⁺ and Na⁺ vacancies V_{Na}⁺ are charge carriers in the FeHCF NDs phase, while
 393 electron e⁻ and holes h⁺ are charge carriers in the rGO phase. The contour map is derived from Gouy-
 394 Chapman profiles. **f**, Schematic of and intercalation storage mechanism for FeHCF MCs/rGO and an
 395 interfacial storage mechanism for FeHCF NDs/rGO with job-sharing storage and transport of ions and
 396 electrons separately. **g**, Dependence of sodium interfacial storage on sodium activity in FeHCF NDs/rGO
 397 nano-composites, where the plot was fitted to the power law function. The power law exponent, *n*, is given
 398 at various voltages. *n* between 3 and 4 is considered to be a reliable fit for charge storage predominantly

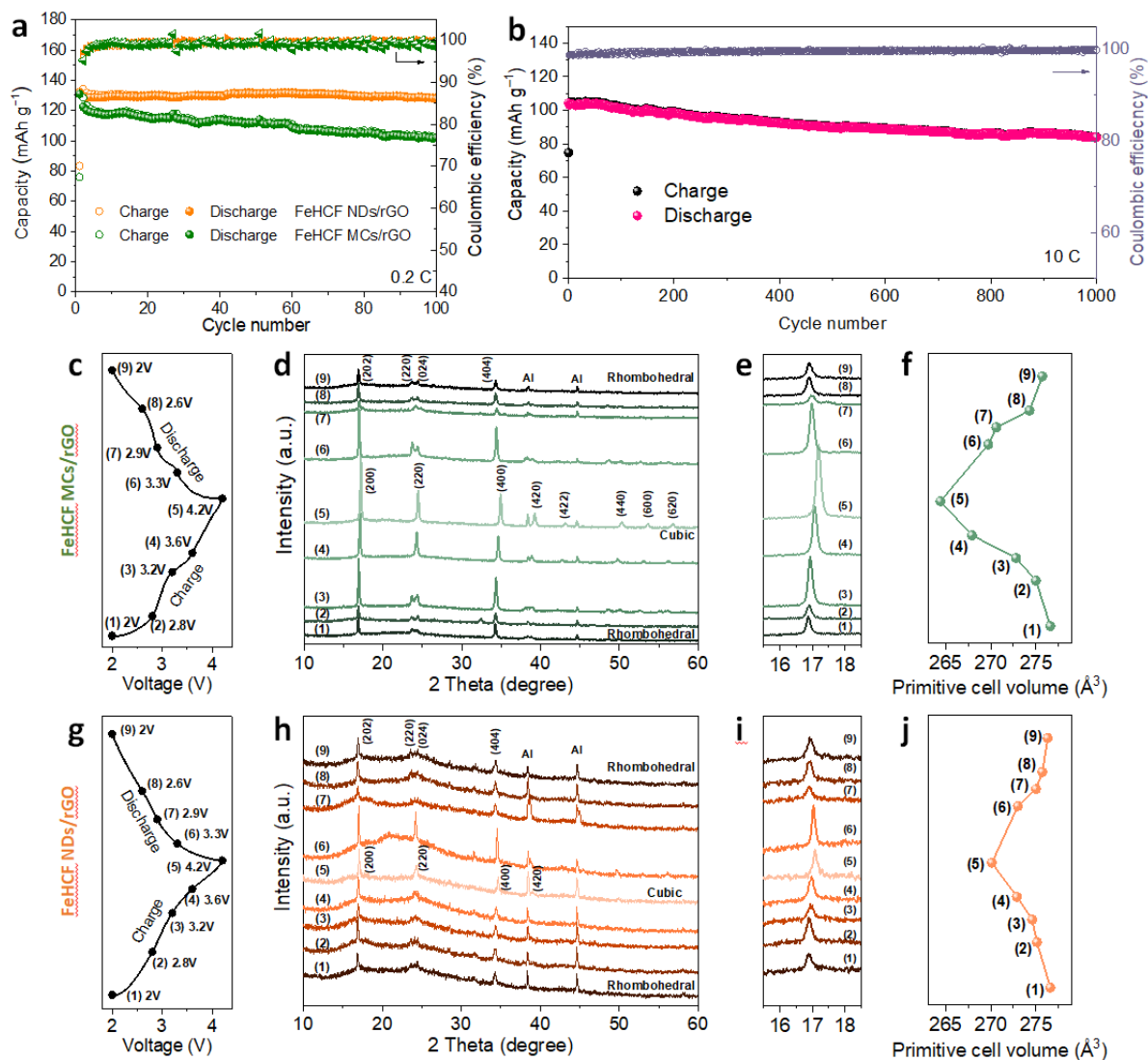
399 in the diffuse layer. **h**, Dependence of $E + nRT \ln Q/F$ on interfacial storage with n values is 3 and 4,
400 respectively. The data shows a good linear fitting in high storage. **i**, Dependence of insertion capacity on
401 the cube length.

402



403

404 **Fig. 4 Reaction kinetics analysis.** **a**, Rate capability of FeHCF NDs/rGO and FeHCF MCs/rGO.
 405 Charge/discharge curves at different current densities for **b** FeHCF NDs/rGO and **c** FeHCF MCs/rGO. **d**,
 406 Comparison of rate capability of other previously reported PBA-based cathode materials. **e**, Log (peak
 407 current) vs. log (scan rate) plots at cathodic and anodic peaks, and the corresponding linear fitting for the
 408 two samples. **f**, Normalized percentage capacitive contributions of the two samples obtained at different
 409 scan rates. **g**, GITT curves and the calculated Na ion diffusion coefficients of the two samples. **h**, The
 410 atomic proportion of Fe^{III} for the two samples at various discharged states after curve-fitting of XPS
 411 spectra. **i**, Schematic summary of the kinetic mechanism where the interface/surface and the interior of
 412 the crystals collaborate effectively.



413

414 **Fig. 5 Cyclic stability and structural evolution analyses.** a, Cycling performance at 0.2 C of FeHCF
 415 MCs/rGO and FeHCF NDs/rGO. b, Long-term cycling performance at 10 C of FeHCF NDs/rGO. Ex-situ
 416 characterizations at different states for FeHCF MCs/rGO and FeHCF NDs/rGO: c, g, charge/discharge
 417 curves; d, h, ex-situ XRD patterns; e, i, enlarged ex-situ XRD patterns; f, j, corresponding normalized
 418 volume variations.

419

Figures

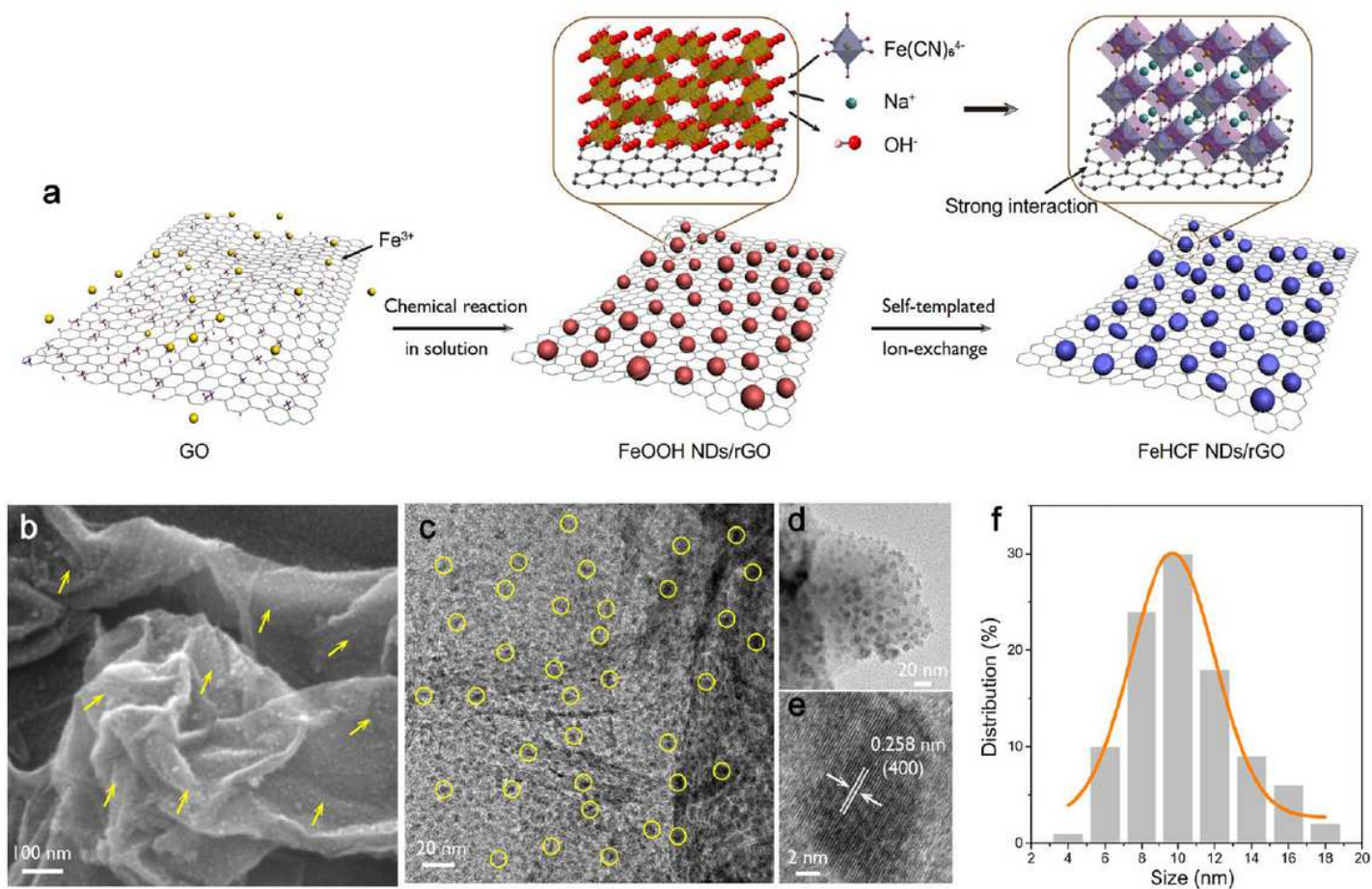


Figure 1

Synthesis process and microstructural analyses of FeHCF NDs/rGO. a, Schematic illustration of the synthesis process by a two-step method. b, SEM image. c, d, TEM images. e, HRTEM image. f, Particle size distribution of FeHCF NDs (200 particles counted).

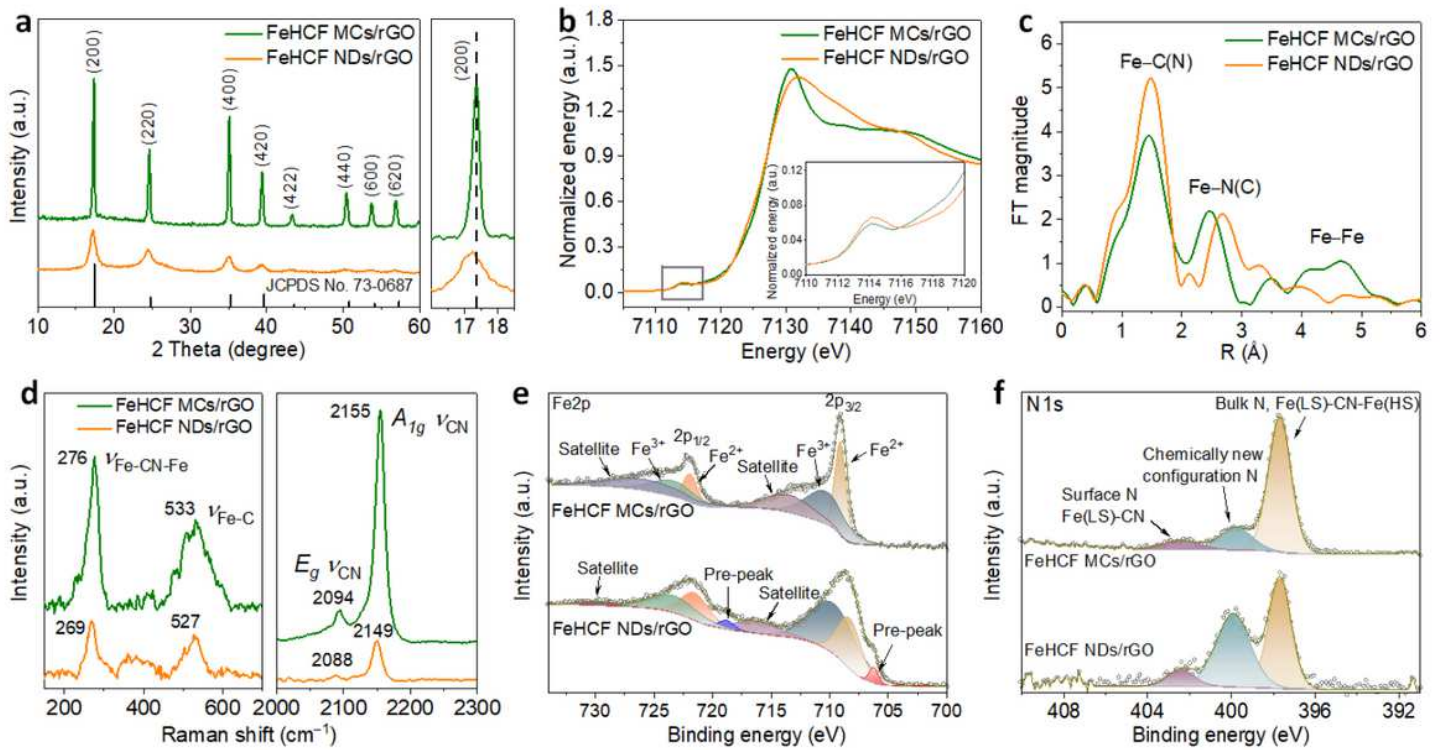


Figure 2

Structure characterizations of FeHCF MCs/rGO and FeHCF NDs/rGO. a, XRD patterns, including an enlargement of the region around the (200) reflection. b, XANES spectra of the Fe K-edge; inset shows the expanded pre-edge region. c, Fourier transformed EXAFS spectra of the Fe K-edge. d, Raman spectra. e, Fe 2p XPS spectra. f, N 1s XPS spectra.

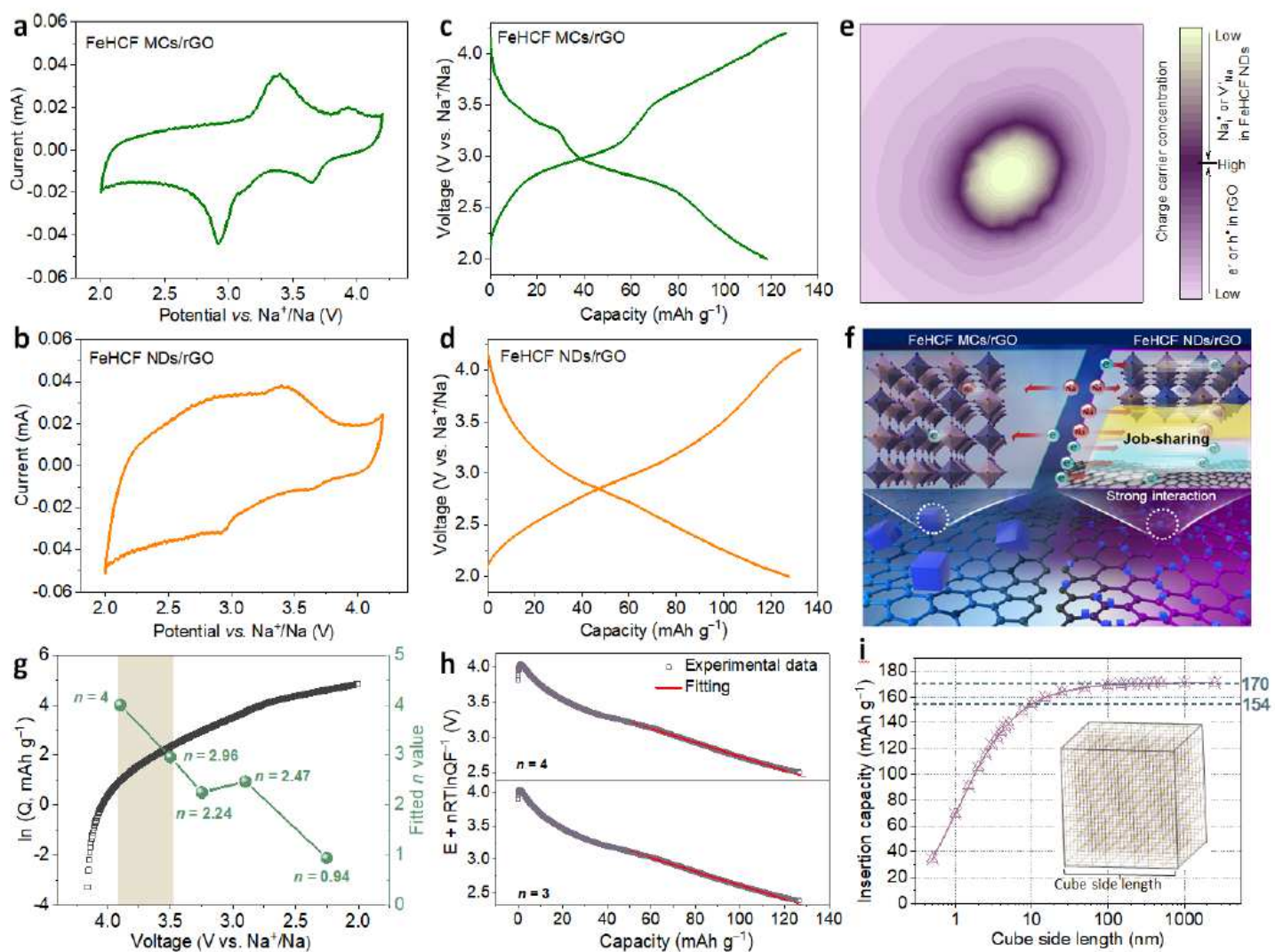


Figure 3

General electrochemical analyses. Typical CV curves at 0.1 mV s^{-1} of a FeHCF MCs/rGO and b FeHCF NDs/rGO. Typical galvanostatic charge/discharge profiles at 0.2 C ($1 \text{ C} = 170 \text{ mA g}^{-1}$) of c FeHCF MCs/rGO and d FeHCF NDs/rGO. e, Visible redistribution of charge carriers at the FeHCF NDs/rGO interface. Na^+ interstitials Na_i^+ and Na^+ vacancies V_{Na} are charge carriers in the FeHCF NDs phase, while electron e^- and holes h^+ are charge carriers in the rGO phase. The contour map is derived from Gouy-Chapman profiles. f, Schematic of and intercalation storage mechanism for FeHCF MCs/rGO and an interfacial storage mechanism for FeHCF NDs/rGO with job-sharing storage and transport of ions and electrons separately. g, Dependence of sodium interfacial storage on sodium activity in FeHCF NDs/rGO nano-composites, where the plot was fitted to the power law function. The power law exponent, n , is given at various voltages. n between 3 and 4 is considered to be a reliable fit for charge storage predominantly in the diffuse layer. h, Dependence of $E + nRT \ln Q/F$ on interfacial storage with n values is 3 and 4, respectively. The data shows a good linear fitting in high storage. i, Dependence of insertion capacity on the cube length.

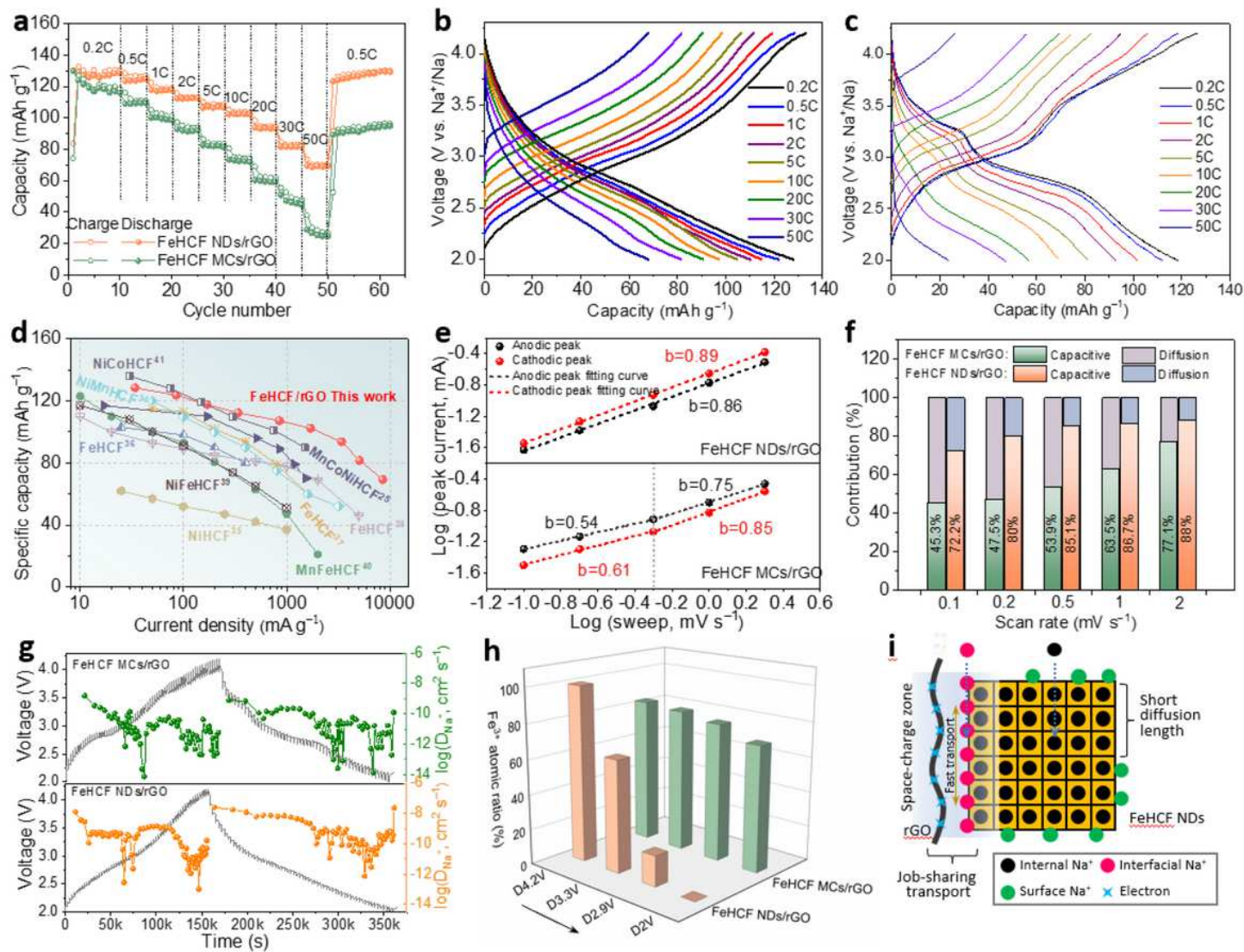


Figure 4

Reaction kinetics analysis. a, Rate capability of FeHCF NDs/rGO and FeHCF MCs/rGO. Charge/discharge curves at different current densities for b FeHCF NDs/rGO and c FeHCF MCs/rGO. d, Comparison of rate capability of other previously reported PBA-based cathode materials. e, Log (peak current) vs. log (scan rate) plots at cathodic and anodic peaks, and the corresponding linear fitting for the two samples. f, Normalized percentage capacitive contributions of the two samples obtained at different scan rates. g, GITT curves and the calculated Na ion diffusion coefficients of the two samples. h, The atomic proportion of Fe for the two samples at various discharged states after curve-fitting of XPS spectra. i, Schematic summary of the kinetic mechanism where the interface/surface and the interior of the crystals collaborate effectively.

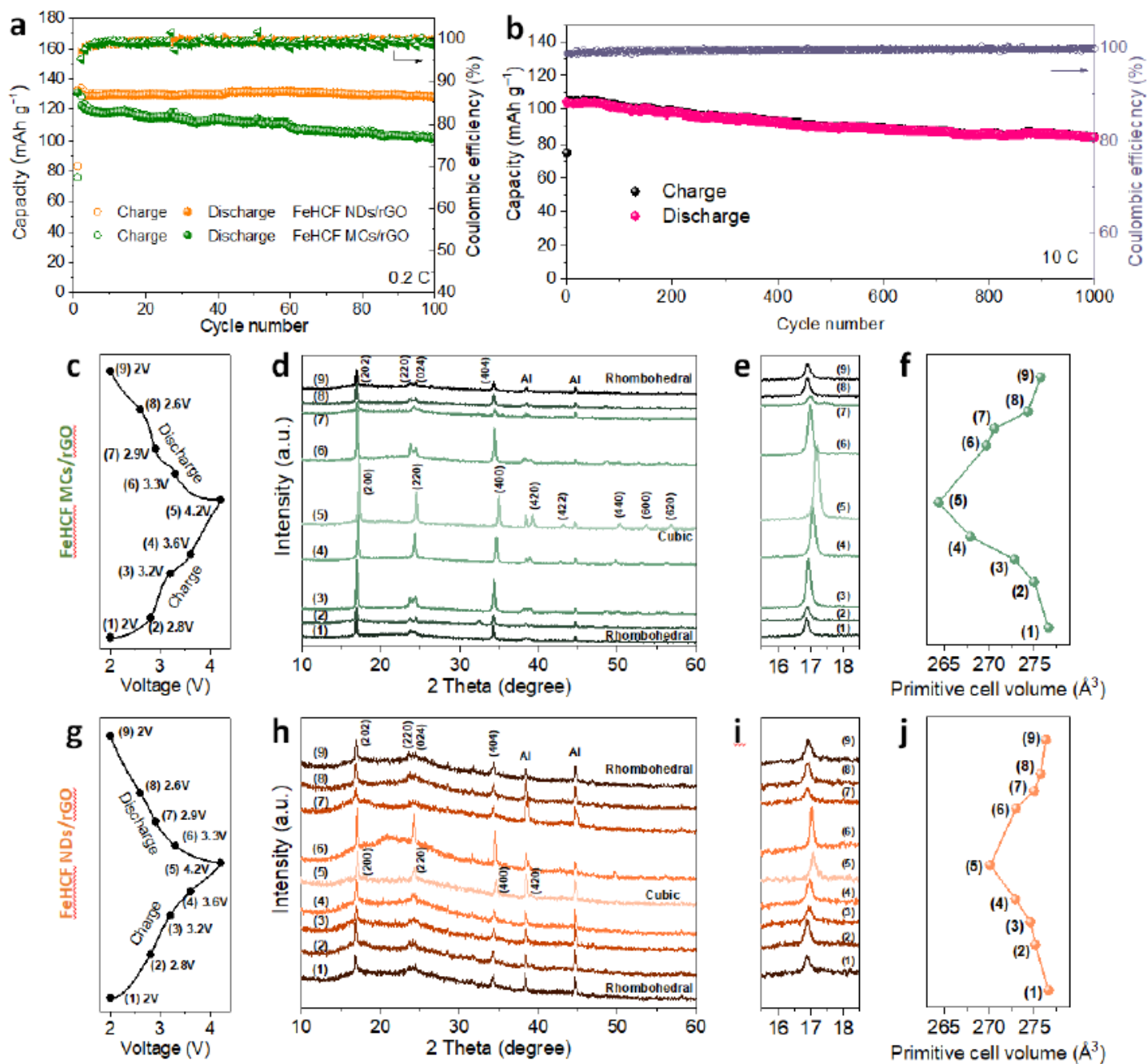


Figure 5

Cyclic stability and structural evolution analyses. a, Cycling performance at 0.2 C of FeHCF MCs/rGO and FeHCF NDs/rGO. b, Long-term cycling performance at 10 C of FeHCF NDs/rGO. Ex-situ characterizations at different states for FeHCF MCs/rGO and FeHCF NDs/rGO: c, g, charge/discharge curves; d, h, ex-situ XRD patterns; e, i, enlarged ex-situ XRD patterns; f, j, corresponding normalized volume variations.

Supplementary Files

This is a list of supplementary files associated with this preprint. Click to download.

- [Supporting information Nature YMKHHW Final1.pdf](#)